Astron. Astrophys. 216, 337–346 (1989)

ASTRONOMY AND ASTROPHYSICS

Technical aspects of the speckle masking phase reconstruction algorithm

E. Pehlemann[1] **and O. von der Lühe**[2, *]

[1] Max-Planck-Institut für Radioastronomie, Auf dem Hügel 69, D-5300 Bonn 1, Federal Republic of Germany
[2] National Solar Observatory**, Sacramento Peak, Sunspot, NM 88349, USA

Received January 4; accepted February 2, 1989

Summary. We discuss technical problems that arise when the full four-dimensional speckle masking algorithm is implemented to reconstruct diffraction-limited two-dimensional images of astronomical objects, with particular emphasis on extended sources. The symmetries of the four-dimensional speckle masking bispectrum are used to relax computer memory requirements of the algorithm without loss of information. Further limits on the bispectrum reduce it to manageable sizes, but imply a loss of information. We discuss various approaches of bispectrum truncation and the consequences for the phase recovery process, and we introduce phase consistency and phase number diagrams as tools for quality assessment of the algorithm and the reconstruction. Different sequences for the phase recovery process are discussed as well. We present sample reconstructions of a point source and of an extended object (a section of the solar photosphere).

Key words: image processing — interferometry — observational methods — seeing

1. Introduction

Since the pioneering work of Labeyrie (1970), a large variety of speckle imaging techniques has been developed to overcome image degradation due to turbulence in the earth's atmosphere (see e.g. Goad, 1987). For image reconstruction of extended objects, like small scale structure on the solar surface, there are basically two promising approaches: the Knox-Thompson technique (Knox and Thompson, 1974) and the speckle masking algorithm (Weigelt, 1977; Weigelt and Wirnitzer, 1983; Lohmann et al., 1983 (hereafter LWW); Bartelt et al., 1984 (hereafter BLW)). For several reasons, speckle masking seems to be the more powerful method:

1. Since images of extended objects often have low contrast ($\Delta I/\bar{I} \approx 1 \ldots 15\,\%$ rms, for solar small scale structure), the high redundancy of phase information inherent in speckle masking increases the signal-to-noise ratio of the reconstruction.
2. When the solar surface is observed, proper motion as well as evolution changes the aspect of the fine structure. These changes can be resolved with today's solar telescopes within periods as little as some 30 seconds (von der Lühe and Zirker, 1988). The number of speckle images that can be combined to a single reconstruction is therefore limited to a few hundred frames, thus making an algorithm with a good signal-to-noise ratio even more important.
3. During the last few years, several publications have pointed out similarities between phase closure techniques and speckle masking (e.g., Roddier, 1986; Cornwell, 1987). It has been proven that speckle masking is well suited to process speckle interferograms obtained with coherent, non-redundant or redundant optical arrays (Reinheimer and Weigelt, 1987). The Knox-Thompson technique fails in this situation, because the information resides in many isolated regions of the Fourier plane.
4. The average effects of anisoplanatism can be described as a convolution in Fourier space (Roddier et al., 1982), causing signal cross-talk between neighbouring frequencies which severely degrades the performance of speckle techniques (von der Lühe, 1985a). Speckle masking is likely to be less sensitive to this effect than the Knox-Thompson technique, because its phase closure relations can be established for distances in Fourier space larger than the anisoplanatism correlation length (von der Lühe and Pehlemann, 1988 (hereafter VDLP)).

Both algorithms, Knox-Thompson and speckle masking, have been applied to a wide variety of astronomical objects. For most of its previous applications, the speckle masking algorithm has been implemented in a modified version, where the reconstruction of the two-dimensional (2D) object image is composed from reconstructions of several one-dimensional (1D) projections (e.g. LWW; Neri and Grewing, 1987). The main advantage of such a procedure is that it avoids the computation of the complete four-dimensional (4D) speckle masking bispectrum and also reduces the number of possible phase recovery sequences. Anyhow, Hofmann and Weigelt (1986) used the intrinsic 4D form of the algorithm. All of these publications deal with objects that consist of one or a few point sources. Reconstructions of extended objects using the Knox-Thompson technique were made by von

Send offprint requests to: E. Pehlemann
* Present address: Institut für Astronomie, ETH-Zentrum, CH-8092 Zürich, Switzerland
** Operated by the Association of Universities for Research in Astronomy, Inc., under contract with the National Science Foundation

der Lühe (1985b, 1987b). Recently, the authors presented the first reconstruction of an extended object using a 4D implementation of the speckle masking algorithm (VDLP).

In the present paper, we address problems that arise with a 4D implementation of the speckle masking algorithm. First, for reasonable sizes of the field of view, the 4D bispectrum requires an amount of computer memory which is impossible to handle. Symmetries inherent in the bispectrum allow to substantially reduce the memory requirements, but the remaining bispectrum section may still be unrealistically large. Therefore, one has to further restrict the bispectrum to a manageable size, a process which we refer to as 'bispectrum truncation'. In addition, large bispectra imply many computations per recovered object phase. The computation time needed for a reconstruction is also remarkably reduced by bispectrum truncation. This is important if time series with many reconstructions are generated of sources that show evolution during observation, as does solar small scale structure. On the other hand, a truncated bispectrum contains less information than the complete bispectrum, and at a certain point, the accuracy to which the object image can be recovered will be compromised. A tradeoff between available computing resources and accuracy of the reconstructed image has therefore to be made. Second, the result of the speckle masking reconstruction process does not only depend on the choice of the bispectrum subset, but also on the sequence with which the elements of this subset are accessed during amplitude and phase recovery. Usage of the same bispectrum subsection and thus of the same image information can result in different reconstructed images, depending on how the elements of the 4D bispectrum are chained up into a linear sequence. Thus the phase recovery sequence needs to be carefully chosen.

We will discuss several approaches to bispectrum truncation and various phase recovery sequences. We also introduce phase consistency and phase number diagrams as tools for quality assessment of both the phase recovery algorithm and the reconstructed image. The effects of the discussed truncation procedures and recovery sequences are demonstrated by sample reconstructions of a point source and an extended source.

2. The 4D speckle masking bispectrum

2.1. Definitions

Consider the Fourier transform $I(\boldsymbol{q})$ of a real-valued image $i(\boldsymbol{x})$. $\boldsymbol{q}$ represents a continuous 2D spatial frequency. If the image is digitized at discrete, equally spaced locations and thus represented by an $N \times N$ matrix of 'pixels', the principal discrete Fourier Spectrum $I(i,j)$ also has $N \times N$ elements. Here, i and j denote integer spatial frequency indices and, for the principal spectrum, are element of the set:

$$\mathscr{PS} := \{-N/2,\ldots,+N/2-1\}. \tag{1}$$

The (constant) direct average frequency component is then at index (0,0). The speckle masking bispectrum is defined as

$$B(\boldsymbol{q},\boldsymbol{p}) = \langle\, I(\boldsymbol{q}) \cdot I(\boldsymbol{p}) \cdot I(-\boldsymbol{q}-\boldsymbol{p}) \,\rangle, \tag{2}$$

or in the discrete form:

$$B(i,j,k,l) = \langle\, I(i,j) \cdot I(k,l) \cdot I(-i-k,-j-l) \,\rangle, \tag{3}$$

where angular brackets denote an average over all speckle images.

We further define the 'bispectrum support', the set of index quadruples for which the bispectrum will be computed, as

$$\mathscr{BS} := \{\, (i,j,k,l) \mid i,k,i+k,j,l,j+l \in \mathscr{PS} \,\}. \tag{4}$$

For symmetry considerations it is convenient to work with a symmetric continuation of the actual bispectrum support, i.e., to increase all upper index bounds from $N/2-1$ to $N/2$. Thus we finally define the symmetry-extended principal spectrum range

$$\mathscr{PS}_{\mathrm{sym}} := \{-N/2,\ldots,+N/2\} \tag{5}$$

and the symmetry-extended bispectrum support

$$\mathscr{BS}_{\mathrm{sym}} := \{\, (\boldsymbol{q},\boldsymbol{p}) \mid \boldsymbol{q}=(i,j), \boldsymbol{p}=(k,l); \; i,k,i+k,j,l,j+l \in \mathscr{PS}_{\mathrm{sym}} \,\}. \tag{6}$$

This extended support has the advantage that the symmetry transformations defined below operate on a closed set of index quadruples.

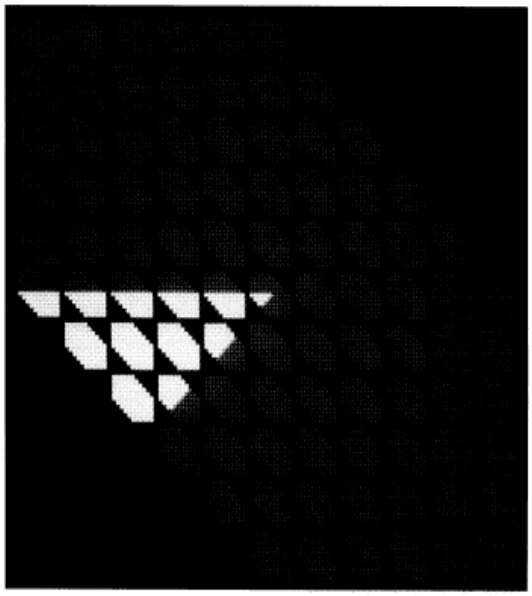

Fig. 1. Bispectrum support $\mathscr{BS}_{sym}$ of a 10×10 pixel data set. Bright squares mark the index quadruples that form the non-redundant subset $\mathscr{NRS}$ defined in Eq. (12).

2.2. Bispectrum representation

If one deals with images and image reconstruction, it is helpful to visualize the quantities that contain the image information. It is hard to display the 4D bispectrum on a 2D piece of paper, but it can be done as follows: Two of the four bispectrum coordinates are chosen to form a 2D 'super'-matrix, its elements being 2D subplanes of the bispectrum. We then have an outer, large coordinate grid for two coordinates and at each grid position an inner, small coordinate grid for the other two coordinates. We find two useful bispectrum representations:

a) outer coordinates i and k
   inner coordinates j and l
b) outer coordinates k and l
   inner coordinates i and j

Representation b) is useful for the first bispectrum truncation method discussed below (Sect. 2.4), while in most of the other cases we prefer representation a). There are, of course, several other solutions to the problem of bispectrum representation. Figure 1 shows the bispectrum of a 10 × 10 pixel data set in representation a).

2.3. Bispectrum symmetries

The inherent symmetries of the speckle masking bispectrum have already been discussed by LWW and BLW. Here we want to present them in a different manner, which is more convenient for practical applications of the algorithm.

We refer to the bispectrum symmetries in form of transformations operating on the (extended) bispectrum support. We define 12 mappings

$$T_{01},\ldots,T_{12} : \mathscr{BS}_{\mathrm{sym}} \rightarrow \mathscr{BS}_{\mathrm{sym}}$$

by

$$\begin{aligned}
T_{01} &: (\boldsymbol{q},\boldsymbol{p}) \mapsto (\boldsymbol{q},\boldsymbol{p})\\
T_{02} &: (\boldsymbol{q},\boldsymbol{p}) \mapsto (\boldsymbol{p},\boldsymbol{q})\\
T_{03} &: (\boldsymbol{q},\boldsymbol{p}) \mapsto (\boldsymbol{q},-\boldsymbol{q}-\boldsymbol{p})\\
T_{04} &: (\boldsymbol{q},\boldsymbol{p}) \mapsto (\boldsymbol{p},-\boldsymbol{q}-\boldsymbol{p})\\
T_{05} &: (\boldsymbol{q},\boldsymbol{p}) \mapsto (-\boldsymbol{q}-\boldsymbol{p},\boldsymbol{q})\\
T_{06} &: (\boldsymbol{q},\boldsymbol{p}) \mapsto (-\boldsymbol{q}-\boldsymbol{p},\boldsymbol{p})\\
T_{07} &: (\boldsymbol{q},\boldsymbol{p}) \mapsto (-\boldsymbol{q},-\boldsymbol{p})\\
T_{08} &: (\boldsymbol{q},\boldsymbol{p}) \mapsto (-\boldsymbol{p},-\boldsymbol{q})\\
T_{09} &: (\boldsymbol{q},\boldsymbol{p}) \mapsto (-\boldsymbol{q},\boldsymbol{q}+\boldsymbol{p})\\
T_{10} &: (\boldsymbol{q},\boldsymbol{p}) \mapsto (-\boldsymbol{p},\boldsymbol{q}+\boldsymbol{p})\\
T_{11} &: (\boldsymbol{q},\boldsymbol{p}) \mapsto (\boldsymbol{q}+\boldsymbol{p},-\boldsymbol{q})\\
T_{12} &: (\boldsymbol{q},\boldsymbol{p}) \mapsto (\boldsymbol{q}+\boldsymbol{p},-\boldsymbol{p})\,.
\end{aligned}$$

Then the following symmetry relations hold:

$$B(T_\alpha(\boldsymbol{q},\boldsymbol{p})) = B(\boldsymbol{q},\boldsymbol{p}) \tag{7a}$$

for $\alpha = 01,\ldots,06$ and all $(\boldsymbol{q},\boldsymbol{p}) \in \mathscr{BS}_{\mathrm{sym}}$ and

$$B(T_\alpha(\boldsymbol{q},\boldsymbol{p})) = B^*(\boldsymbol{q},\boldsymbol{p}) \tag{7b}$$

for $\alpha = 07,\ldots,12$ and all $(\boldsymbol{q},\boldsymbol{p}) \in \mathscr{BS}_{\mathrm{sym}}$, where the star denotes complex conjugation. The validity of these symmetry relations can easily be prooved, e.g.:

$$\begin{aligned}
B(T_{05}(\boldsymbol{q},\boldsymbol{p})) &= B(-\boldsymbol{q}-\boldsymbol{p},\boldsymbol{q})\\
&= \langle\, I(-\boldsymbol{q}-\boldsymbol{p})\cdot I(\boldsymbol{q})\cdot I(\boldsymbol{q}+\boldsymbol{p}-\boldsymbol{q})\,\rangle\\
&= \langle\, I(-\boldsymbol{q}-\boldsymbol{p})\cdot I(\boldsymbol{q})\cdot I(\boldsymbol{p})\,\rangle\\
&= \langle\, I(\boldsymbol{q})\cdot I(\boldsymbol{p})\cdot I(-\boldsymbol{q}-\boldsymbol{p})\,\rangle\\
&= B(\boldsymbol{q},\boldsymbol{p})
\end{aligned} \tag{7c}$$

or

$$\begin{aligned}
B(T_{09}(\boldsymbol{q},\boldsymbol{p})) &= B(-\boldsymbol{q},\boldsymbol{q}+\boldsymbol{p})\\
&= \langle\, I(-\boldsymbol{q})\cdot I(\boldsymbol{q}+\boldsymbol{p})\cdot I(\boldsymbol{q}-\boldsymbol{q}-\boldsymbol{p})\,\rangle\\
&= \langle\, I(-\boldsymbol{q})\cdot I(\boldsymbol{q}+\boldsymbol{p})\cdot I(-\boldsymbol{p})\,\rangle\\
&= \langle\, I(-\boldsymbol{q})\cdot I(-\boldsymbol{p})\cdot I(\boldsymbol{q}+\boldsymbol{p})\,\rangle\\
&= \langle\, I^*(\boldsymbol{q})\cdot I^*(\boldsymbol{p})\cdot I^*(-\boldsymbol{q}-\boldsymbol{p})\,\rangle\\
&= \langle\, I(\boldsymbol{q})\cdot I(\boldsymbol{p})\cdot I(-\boldsymbol{q}-\boldsymbol{p})\,\rangle^*\\
&= B^*(\boldsymbol{q},\boldsymbol{p})\,.
\end{aligned} \tag{7d}$$

Let

$$\mathscr{T} := \{T_{01},\ldots,T_{12}\} \tag{8}$$

and

$$\mathscr{G} := (\mathscr{T},\circ)\,, \tag{9}$$

where the law of composition $\circ$ denotes succession of mappings. It can then be shown that $\mathscr{G}$ is a non-abelian group (with T_{01} being the group identity). The practical benefit from this fact is that each symmetry transformation has an inverse. Furthermore, the group structure of $\mathscr{G}$ reveals two different types of symmetries: Transformations $T_{01},\ldots,T_{06}$ originate in the symmetry of the bispectrum definition itself and apply to real and complex data, while transformations $T_{07},\ldots,T_{12}$ are applicable for real data only, because they make use of the hermiticity of the Fourier transform. This difference is easily seen in the above examples. Now let

$$\begin{aligned}
\mathscr{H}_1 &:= (\{T_{01},\ldots,T_{06}\},\circ)\,,\\
\mathscr{H}_2 &:= (\{T_{01},T_{07}\},\circ)\,.
\end{aligned} \tag{10}$$

Then $\mathscr{G}$ is the product of these two subgroups, i.e., we have

$$\mathscr{G} = \mathscr{H}_1 \otimes \mathscr{H}_2\,. \tag{11}$$

Subgroup $\mathscr{H}_1$ is isomorphic to $\mathscr{S}_3$, the symmetric group of degree 3 (permutations on a set of 3 elements), while subgroup $\mathscr{H}_2$ is isomorphic to $\mathscr{Z}_2$, the cyclic group of order 2 (arithmetic modulo 2).

Subgroup $\mathscr{H}_1$ can be created by transformations T_{02} and T_{06}, while subgroup $\mathscr{H}_2$ can be created by transformation T_{07}. This corresponds exactly to the description by LWW and BLW.

2.4. Bispectrum memory use

One crucial problem when implementing the 4D speckle masking algorithm is the size of the bispectrum. For images with typically 128 × 128 pixel, $\mathscr{BS}$ has $9/16 \cdot 128^4 = 150{,}994{,}944$ elements. (The other $7/16 \cdot 128^4$ index combinations correspond to values of $i+k$ or $j+l$ outside the principal spectrum range $\mathscr{PS}$). Assuming 8 byte complex bispectrum values, this corresponds to 1152 Mbyte of memory - far too much for almost every computer. It is therefore essential to reduce the size of the bispectrum.

The first approach is to apply the symmetry properties of the bispectrum. Due to the existence of the 12 symmetry relations, the bispectrum decomposes to 12 non-redundant segments with very little overlap. So only about 1/12 of the $9/16 \cdot N^4$ bispectrum elements need actually to be computed and stored in memory, without loss of any information. Figure 1 shows one possible choice of such a non-redundant subset of the bispectrum. It is described as

$$\begin{aligned}\mathcal{NRS} := \{\,(i,j,k,l) \mid\ & i = -N/2,\ldots,0;\\ & k = -N/4,\ldots,0;\\ & k \geq i;\\ & i+k \geq -N/2;\\ & j,l,j+l \in \mathcal{PS};\\ & l \geq j \quad \text{if} \quad k = i;\\ & l \leq 0 \quad \text{if} \quad k = 0\,\}.\end{aligned} \tag{12}$$

The exact number of elements in $\mathcal{NRS}$ is

$$\frac{3}{64}N^4 + \frac{3}{32}N^3 + \frac{1}{2}N^2 + \frac{1}{2}N + 1$$

or 98 Mbyte for image frames of 128 × 128 pixel.

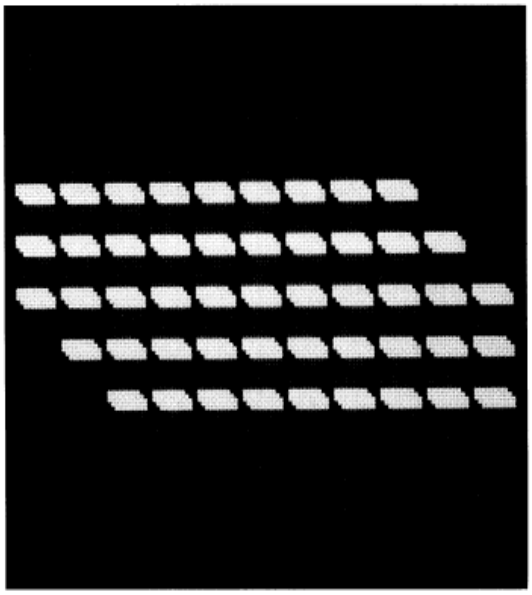

Fig. 2. Bispectrum support $\mathcal{BS}_{sym}$ of a 10 × 10 pixel data set. Bright squares mark the index quadruples that belong to the bispectrum support truncated corresponding to Eq. (13) with a truncation parameter $M = 2$.

In most cases it will be necessary to further reduce the bispectrum size. We call this process truncation of the bispectrum. Bispectrum truncation implies loss of image information. The question arises which parts of the bispectrum should be kept and which elements should be dropped. There are at least three different aspects:

1. From theoretical modeling of the speckle transfer function (LWW; von der Lühe, 1985c) it is known that the bispectrum areas near the axes $\boldsymbol{q} = 0$, $\boldsymbol{p} = 0$ and $\boldsymbol{q} + \boldsymbol{p} = 0$ have highest signal-to-noise ratio.
2. To overcome the effects of anisoplanatism, it is desirable to use index combinations corresponding to large values of $\boldsymbol{q}$, $\boldsymbol{p}$ and $\boldsymbol{q} + \boldsymbol{p}$.
3. For simplicity of computational memory-mapping, the selected areas of the bispectrum should not be too 'porous'; they should consist of a few contiguous patches.

It is obvious that these aspects conflict with each other. One has to find a compromise which may depend on the circumstances of the special application. E.g., Hofmann and Weigelt (1986) truncated the bispectrum to 5 % of its size, using the parts near the axes for their reconstruction of HD 97950 AB.

So far, we used two different methods of bispectrum truncation. The first and simpler method is to restrict the k and l indices of the complete bispectrum support $\mathcal{BS}$ (without making use of the symmetries) to magnitudes less than an adjustable parameter M:

$$|k|, |l| = 0, \ldots, M\,. \tag{13}$$

The speckle masking algorithm then becomes similar to a sequence of several Knox-Thompson reconstructions. This method allows to easily test and compare various phase recovery sequences (see below). Our sample reconstructions of solar granulation showed $M = 5$ to be an optimal choice (see Fig. 7). The quality of the reconstruction increases remarkably when M is raised from 1 to 5, an effect which is probably due to the better correction of anisoplanatism. Further increase of M does not affect the result any more. This may be due to the low signal-to-noise ratio of bispectrum information with large values of $\boldsymbol{q}$, $\boldsymbol{p}$ or $\boldsymbol{q} + \boldsymbol{p}$. The bispectrum of an 128 × 128 pixel data set, truncated with $M = 5$, has a size of 15 Mbyte. The bispectrum elements accessed with this method are shown in Fig. 2.

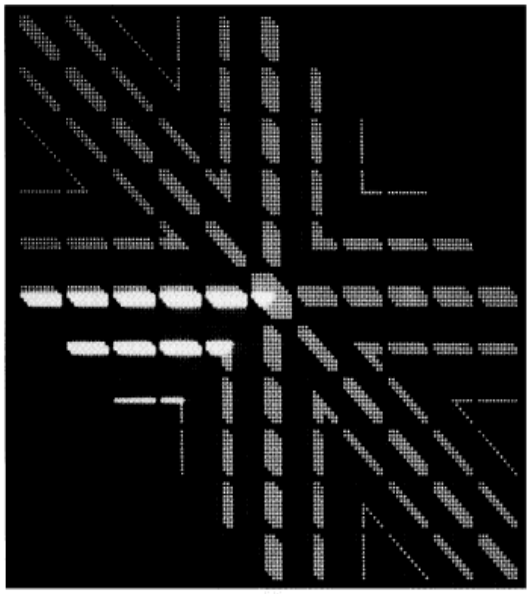

Fig. 3. Bispectrum support $\mathcal{BS}_{sym}$ of a 10 × 10 pixel data set. Bright squares mark the index quadruples that belong to the nonredundant bispectrum subset truncated corresponding to Eq. (14) with a truncation parameter $M = 2$. Light grey squares mark the index quadruples that can be accessed from this subset via the symmetry transformations $T_{01}, \ldots, T_{12}$ of sect. 2.3.

The second method employs both truncation and bispectrum symmetries. It allows to reduce the bispectrum size to a few Mbytes and therefore to run the 4D speckle masking algorithm

on minicomputers like a VAX. Memory mapping becomes more complicated if only the desired bispectrum subset is to be stored in a linear array. We take the non-redundant subset $\mathcal{NRS}$ from Eq. (12) and further impose the restrictions

$$k = 0, \ldots, -M \quad \text{and} \quad |l| = 0, \ldots, M - |k| \,. \tag{14}$$

There are many gaps between the bispectrum areas that can be accessed by applying the symmetry transformations on this subset; even not all bispectrum elements which obey (14) (but belong to other parts of $\mathcal{BS}$ than $\mathcal{NRS}$) are known (see Fig. 3). This complicates the phase recovery sequence, but there is still enough information to recover all Fourier phases.

Table 1 summarizes the bispectrum memory needs for different image sizes and truncation methods. There is, of course, an almost unlimited number of other bispectrum truncation methods. The influence of the selected subset on the resulting reconstruction will be subject to further investigation.

Table 1. Size of the speckle masking bispectrum for different image sizes. We assume that bispectrum elements are stored as 8 byte complex numbers.

Bispectrum subset	Size in Mbyte for images of		
	64 × 64 pixels	128 × 128 pixels	256 × 256 pixels
all N^4 elements	128.0	2048.0	32768.0
$\mathcal{BS}$ (see Eq. (4))	72.0	1152.0	18432.0
$\mathcal{NRS}$ (see Eq. (12))	6.2	97.6	1548.3
truncated, $M = 10$	11.6	50.7	211.6
(see Eq. (13)) $M = 5$	3.5	14.5	59.2
truncated, $M = 10$	1.5	6.7	28.6
(see Eq. (14)) $M = 5$	0.5	2.1	8.8

3. Phase recovery algorithms

Once it is clear which bispectrum elements we want to reference for recovery of the Fourier phase values, we now have to define in which sequence they shall be referenced. This means that we have to extend the considerations of BLW (Sect. IV) to the 4D case. For simplicity, we consider the recovery of Fourier phases only; other methods can be used for amplitude recovery. If the amplitudes are also to be reconstructed by the speckle masking algorithm, similar considerations apply to this procedure.

3.1. *Phase consistency and phase number diagrams*

Fourier phases are recovered using the phase closure equation

$$e^{i\phi(i+k,j+l)} = e^{i\phi(i,k)} \cdot e^{i\phi(j,l)} \cdot e^{-i\Phi(i,j,k,l)} \,, \tag{15}$$

where ϕ is the object phase (the Fourier phase of the final reconstructed image) and Φ is the bispectrum phase. It is convenient to use complex phasors of unity magnitude to represent the phase values, because ambiguities of $\pm\pi$ that can occur when phase values are averaged directly, are avoided in this way.

During the recovery procedure, a certain number of bispectrum elements will contribute to a given element of the object phase at, say, index (m, n), because several combinations of indices i, j, k, l satisfy the truncation condition and result in $i + k = m$, $j + l = n$. For each of these index combinations, a phase closure relation (15) can be established and will result in an individual phasor value $e^{i\phi_\beta(m,n)}$. We should note that we directly average all these phasors without application of any weighting criteria (see Freeman et al. (1988) for a discussion of weighting techniques). The number of these individual phasor values will be referred to as the 'phase number' function:

$$\mathrm{num}(m, n) := \mathrm{card}\left\{ e^{i\phi_\beta(m,n)} \mid \beta = 1, 2, \ldots \right\} . \tag{16}$$

(The card function returns the number of elements in a set.)

The final (averaged) value of the Fourier phase is obtained from the sum of all individual complex phasors. From this sum we also derive a quantity that we call the 'phase consistency':

$$\mathrm{con}(m, n) := \left| \frac{1}{\mathrm{num}(m, n)} \cdot \sum_{\beta=1}^{\mathrm{num}(m,n)} e^{i\phi_\beta(m,n)} \right| . \tag{17}$$

This phase consistency is closely related to the variance of the complex phasors:

$$\begin{aligned} \mathrm{var}(e^{i\phi_\beta(m,n)}) &= \left\langle \left| e^{i\phi_\beta(m,n)} - \langle e^{i\phi_\beta(m,n)} \rangle \right|^2 \right\rangle \\ &= \left\langle \left| e^{i\phi_\beta(m,n)} \right|^2 \right\rangle - \left| \langle e^{i\phi_\beta(m,n)} \rangle \right|^2 \\ &= 1 - \mathrm{con}(m, n)^2 \,. \end{aligned} \tag{18}$$

If all complex phases that contribute to a given combination of indices (m, n) are equal, the value of the consistency function is 1. The consistency function will be much smaller than 1 if the phases are randomly distributed. Thus a consistency near 1 indicates phase values of high quality, and a poor signal-to-noise ratio will result in a consistency of almost zero.

Obviously, both phase number and phase consistency functions should be symmetric in $\boldsymbol{q}_x$ and $\boldsymbol{q}_y$ directions; i.e.,

$$\left.\begin{aligned} \mathrm{num}(m, n) &= \mathrm{num}(n, m) \\ \mathrm{con}(m, n) &= \mathrm{con}(n, m) \end{aligned}\right\} \quad \text{for all } m \text{ and } n \,. \tag{19}$$

Asymmetries of the phase number function indicate a poor phase recovery sequence.

Aside from the phase recovery procedure, the shape of the phase consistency function depends on the quality of the signal, and thus helps to identify areas in the Fourier domain with poorly recovered phases. If both seeing conditions and statistics of the structure are isotropic, one would expect the phase consistency be radially symmetric about the frequency origin, with decreasing values for increasing spatial frequencies. Hence, we consider phase consistency diagrams very useful tools for assessing the quality of a reconstruction.

3.2. Sequence of bispectrum access

The simplest way to sequentially access elements of a 4D array would be to use four simple interlocked loops:

```
DO  l=-N/2,+N/2-1,+1
  DO  k=-N/2,+N/2-1,+1
    DO  j=-N/2,+N/2-1,+1
      DO  i=-N/2,+N/2-1,+1
        ...
      END DO
    END DO
  END DO
END DO
```

But the recursion has to start from the initial values at spatial frequencies (1,0) and (0,1) which can be initialized from the direct average of the Fourier transforms. Care has also to be taken that no phase value is referenced on the right hand side of Eq. (15) before it has been computed on the left hand side earlier. Third, it is desirable to compute as many individual phase values as possible before the phase is referenced for computation of other Fourier phases. Therefore it is the best to start with indices near zero and to keep them small as long as possible.

In addition we want to avoid an m/n-asymmetry of the phase consistency diagram which arises if loops over $\boldsymbol{q}_x$ and $\boldsymbol{q}_y$ indices are simply interlocked. For these reasons we developed a more sophisticated sequence of bispectrum referencing which we call the 'Octagon Method':

First consider only two of the four loops. Let us name their indices m and n. We keep the principal values of m and n inside the triangle

$$\begin{aligned} &m = 0, -1, \ldots, -\mathrm{N}/2\,, \\ &n = 0, -1, \ldots, m\,. \end{aligned} \tag{20}$$

For each combination of these principal values of m and n, we process the eight index combinations

$$\begin{aligned} &(+m,+n),(-m,-n),(+m,-n),(-m,+n)\,, \\ &(+n,+m),(-n,-m),(-n,+m),(+n,-m)\,. \end{aligned}$$

(For illustration see Fig. 4.) If $m = 0, n = 0$ or $m = n$, the number of combination reduces to four or even to one (in the case $m = n = 0$). These eight index combinations form the corners of an octagon in the m/n-plane and are meant as an approximation to a circle of elements with the same distance from the origin.

The same procedure is used for the two other indices, resulting in another set of up to eight index combinations. With one pair of loops inside the other, we process up to 8×8 index combinations for fixed values of the four primary induction variables. For each of these index combinations it must be verified whether the indices are inside the known bispectrum range $\mathcal{BS}$ (or $\mathcal{NRS}$) or not.

There are several possibilities to select the two loop pairs. One is to combine the i and k loops to one octagon and the j and l loops to the other. In this case, the consistency diagram shows drastic asymmetry (see Fig. 6). A better way is to combine i and j indices to form one octagon and the k and l indices to form the other one. If truncation method (13) is used, there is even a difference if the truncated loops form the inner or outer pair. The best combination we found so far is to put the truncated k/l octant loops inside the i/j octant loops.

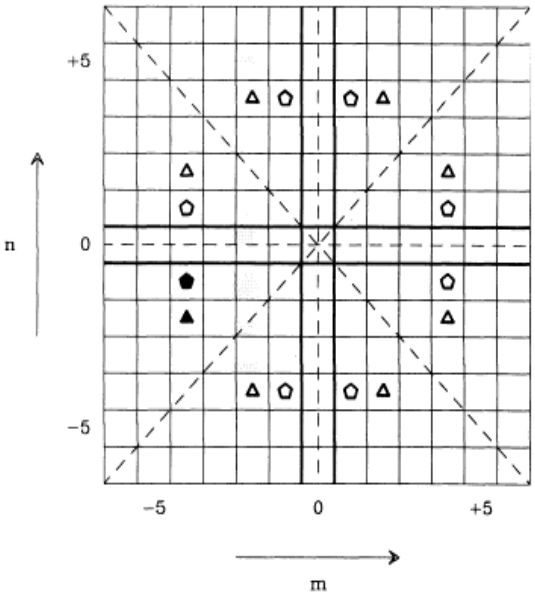

Fig. 4. Illustration of the Octagon Method. The triangle of principal values of the loop indices m and n described in Eq. (20) is that one containing the filled triangle and pentagon. All eight index pairs marked by pentagons are processed with one fixed combination (m,n) of principal index values. Then this combination is changed, and another eight index pairs are processed, e.g. those marked by triangles.

If the bispectrum size is reduced by taking advantage of the symmetry transformations, additional care has to be taken to avoid an asymmetric phase number diagram. To explain this let us assume that the bispectrum is reduced to $\mathcal{NRS}$ and that all of its values are to be accessed during phase recovery. Let us rewrite Eq. (15) in a little different form:

$$\mathrm{e}^{\mathrm{i}\phi(i+k,j+l)} = \mathrm{e}^{\mathrm{i}\phi(i,k)} \cdot \mathrm{e}^{\mathrm{i}\phi(j,l)} \cdot \mathrm{e}^{-\mathrm{i}\Phi(I,J,K,L)}\,, \tag{15'}$$

where i,j,k,l and I,J,K,L denote two different index sets. Since the bispectrum is known only for the index combinations of $\mathcal{NRS}$, the I,J,K,L indices have to be restricted to this index range. If we would restrict the i,j,k,l indices to the same range, we would get a highly asymmetric phase number diagram, because the values of the index pairs (i,k) are highly restricted while there are only negligible restrictions for the values of (j,l) index pairs at the edges of the (i,k) range (confirm Eq. (12)). These asymmetries have a remarkable effect on the final reconstruction: It tends to become symmetric with respect to the image center! If the object is a single star positioned with an offset from the center, the reconstructed image shows two stars, with a difference in position angle (measured from the center of the image) of 180° (see Fig. 6).

Thus it is important to use all index combinations of the complete bispectrum support $\mathcal{BS}$ for the i,j,k,l indices. For each of these combinations, one has to find the corresponding index combination (I,J,K,L) which lies inside $\mathcal{NRS}$ and is related to (i,j,k,l) by one of the 12 symmetry transformations:

$$\begin{aligned} (I,J,K,L) &= T_\alpha^{-1}(i,j,k,l) \\ &= T_{\alpha'}(i,j,k,l)\,. \end{aligned} \tag{21}$$

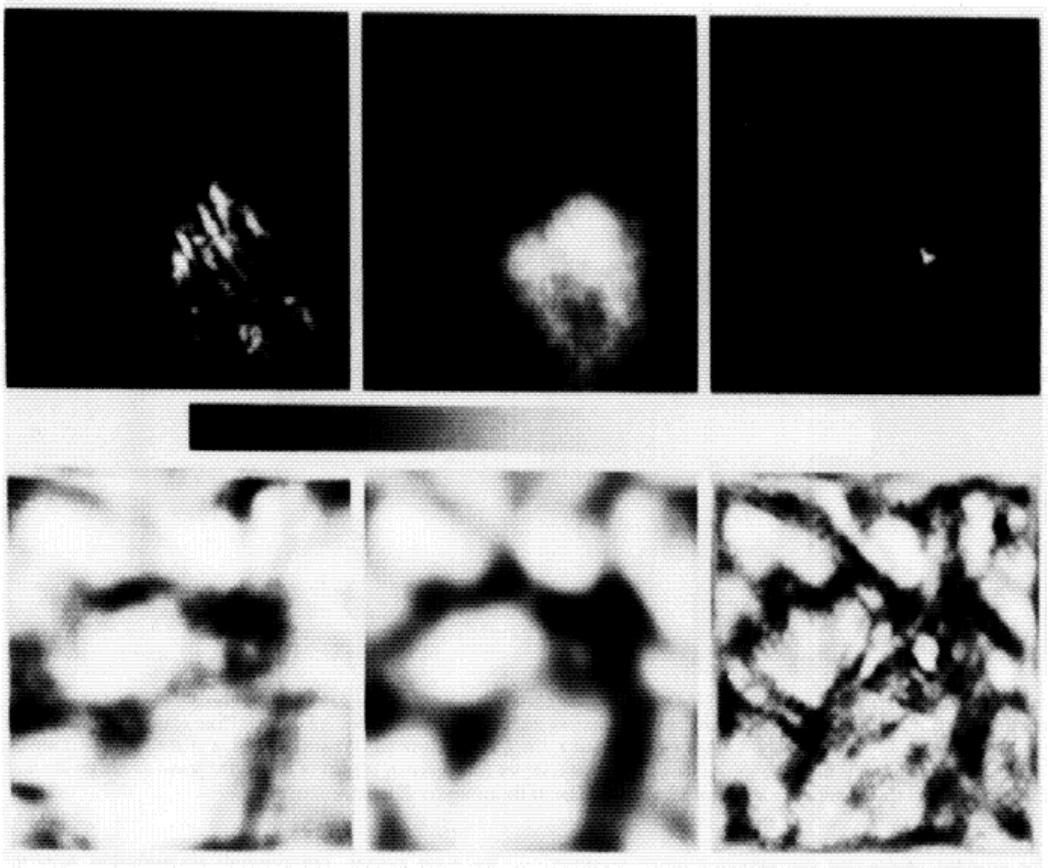

Fig. 5. Results of the speckle masking image reconstruction process. Top row: Point source (β Scorpii). Bottom row: Extended source (solar granulation fine structure). Left column: Sample speckle images. Center column: Direct averages of all frames, corresponding to a long-time exposure. Right column: Final speckle masking reconstructions, obtained from a bispectrum truncated corresponding to Eq. (13) with a truncation parameter $M = 5$. All six images are individually scaled; brightness and contrast are thus not comparable between different images. The reconstruction of the solar granulation data was apodised with a Hamming window (covering the outer 25 % of all pixels) and corrected for seeing.

(This means that each element of $\mathcal{NRS}$ will be referenced 12 times.) This way the artificial symmetry in the final reconstruction and the asymmetries of the phase number and consistency diagrams can be avoided. The determination of the correct transformation index α' from I,J,K,L is straightforward.

4. Results

4.1. Image reconstruction procedure

Before we show sample reconstructions to illustrate the points discussed in the preceding sections, we describe in more detail how we apply the speckle masking method. The major steps are:

4.1.1. Raw data pre-processing

Some pre-processing is done before the reconstruction process. It includes correction for dark current and gain table, intensity normalization, removal of bilinear trends in the individual speckle frames, and recentering by means of a cross-correlation algorithm (von der Lühe, 1983).

4.1.2. Bispectrum computation

The data are Fourier-transformed frame by frame. From the transforms, the individual (truncated) bispectra are calculated and accumulated to obtain the (truncated) speckle masking bispectrum as defined in Eq. (3).

4.1.3. Amplitude recovery

The Fourier amplitudes of the reconstruction are obtained from the bispectrum via Labeyrie's technique: Setting $\boldsymbol{p} = \mathbf{0}$ in Eq. (2) results in

$$B(\boldsymbol{q}, \mathbf{0}) = I(\mathbf{0}) \cdot \langle\, |I(\boldsymbol{q})|^2 \,\rangle\,. \tag{22}$$

The average power spectrum, which is used in the Labeyrie method, is contained in the bispectrum in this manner.

The 'raw' amplitudes still require correction for the speckle transfer function (STF). We use the Spectral Ratio Technique (von der Lühe, 1987a) to estimate Fried's parameter r_0 from the speckle data set and then correct the raw amplitudes with a corresponding model STF (Korff, 1973).

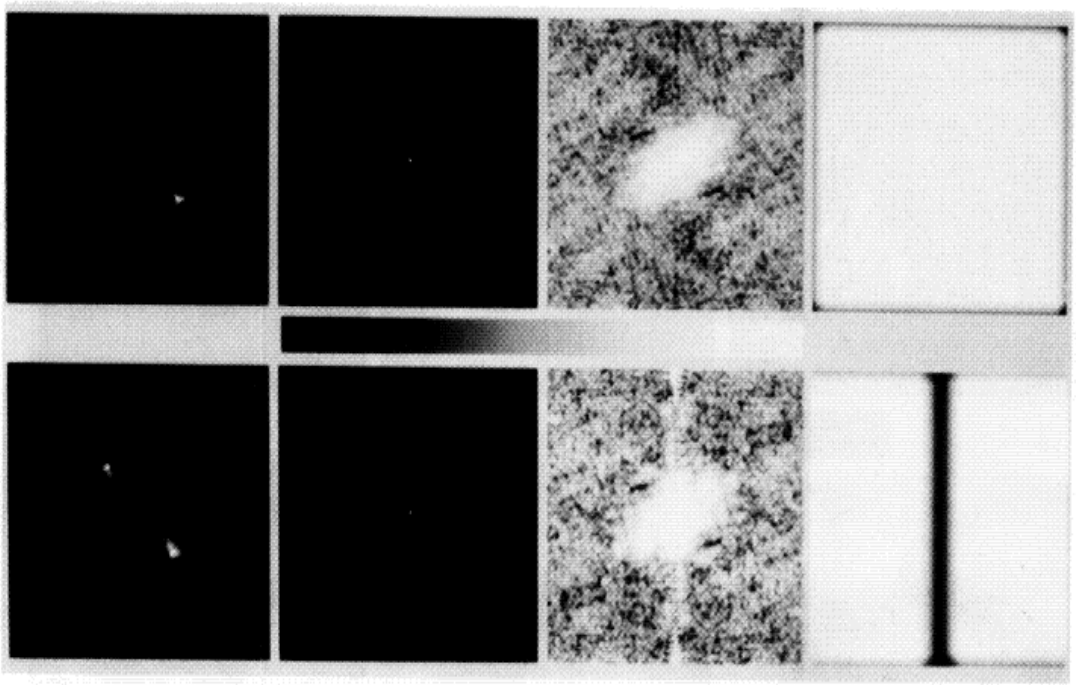

Fig. 6. Effects of the phase recovery sequence on the phase number and phase consistency diagrams. Same point source data set as top row of Fig. 5. Colums from left to right: 1st column: Speckle masking reconstructions. 2nd column: Power spectra. 3rd column: Phase consistency diagrams. 4th column: Phase number diagrams. Bottom row: Both the i,j,k,l and I,J,K,L index sets of Eq. (15′) are restricted to $\mathcal{NRS}$. Top row: Only the I,J,K,L indices are restricted in that way, whereas the i,j,k,l indices cover the full bispectrum support of Eq. (4). The power spectra are identical. Note the second star in the reconstruction at bottom left which is added by the asymmetry of the algorithm.

For extended objects, the raw reconstruction is apodised with a Hamming window prior to amplitude correction in order to reduce the influence of high spatial frequencies caused by discontinuities at the image boundary.

4.1.4. Phase recovery

Using the phase recovery sequences discussed in Sect. 3, the Fourier phases of the reconstruction are obtained from the bispectrum. These phase values need not be seeing-corrected. We neglect deterministic effects of telescope aberrations at this moment.

4.1.5. Image reassembly

The final reconstruction is obtained from the corrected Fourier amplitudes and the reconstructed Fourier phases via an inverse Fourier transform.

4.2. *Data sets*

To investigate the influence of different bispectrum truncation strategies and various phase recovery sequences and to test the performance of the algorithm, we used two different sets of speckle data:

1. A set of 51 speckle images of β Scorpii, 128 × 128 pixel, taken with the Mc Math telescope at Kitt Peak by P. Nisenson (Center for Astrophysics). This set serves as a point source example. The top row of Fig. 5 shows a sample frame, the direct average, and a sample reconstruction. Note the asymmetry of the direct average, which may be caused either by instrumental aberrations or by seeing anisotropy in this very limited data set.
2. A set of 100 speckle frames of a 5.″2 × 5.″2 field (128 × 128 pixel) of the solar photosphere. This set was taken with the 76 cm vacuum tower telescope at NSO - Sacramento Peak. A bandpass of 5 nm width was centered at 585 nm. Frames were taken every 0.6 s with an exposure of 4 ms. We estimated a Fried parameter r_o of 13.3 cm during this run, which is rather good for day-time seeing. The bottom row of Fig. 5 shows a sample frame, the direct average, and a reconstructed picture.

4.3. *Sample reconstructions*

Figs. 5 – 7 show sample reconstructions made from the two data sets. The reconstructions of β Scropii were done without correction for the STF. This results in a reconstruction that shows the recovered object on top of a smooth background with the extent of the average seeing disk. We found it not necessary to correct for the STF in this rather technical study which is mainly concerned with the phase recovery method. The reconstructions of solar data are all corrected for the STF.

Figure 6 demonstrates the effect of the phase recovery sequence on the reconstruction and the diagnostic diagrams. Results where indices I, J, K, and L were restricted to $\mathcal{NRS}$ while indices i, j, k, and l cover the full bispectrum support are shown in the top row. Both index groups were restricted to $\mathcal{NRS}$ for the results shown in the bottom row.

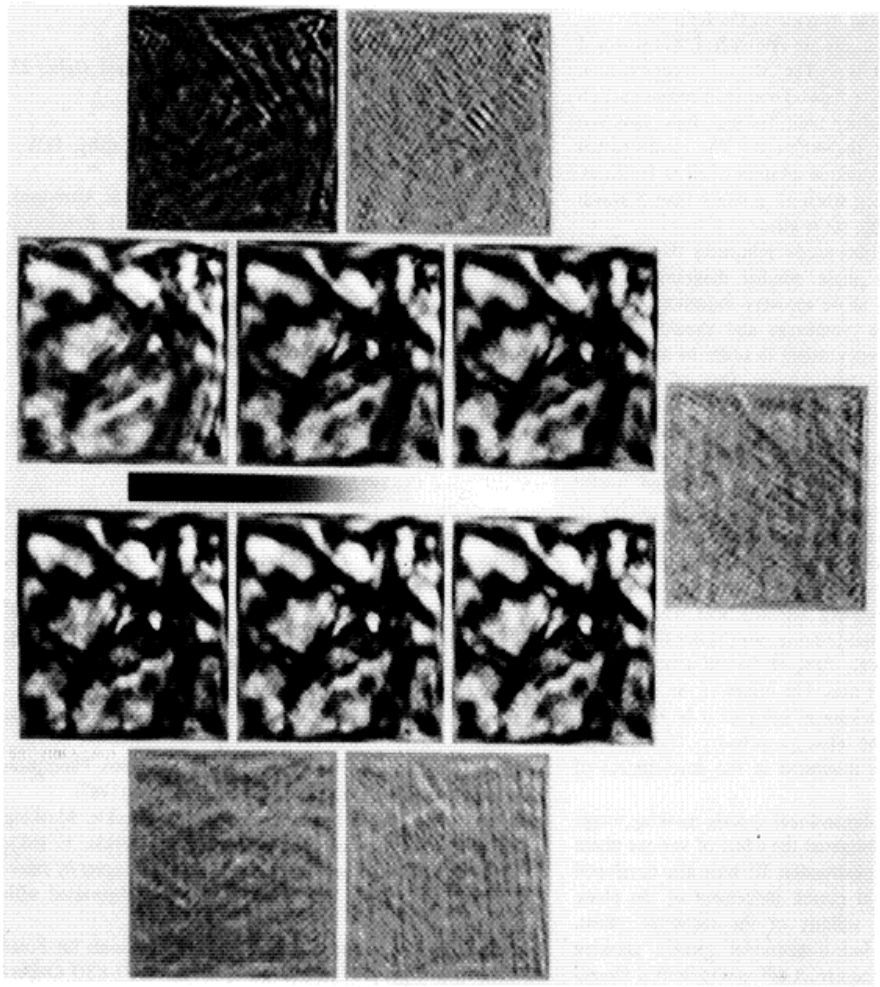

Fig. 7. Effects of bispectrum truncation. The center rows show speckle masking reconstructions of solar granulation fine structure. The other five images are difference images of the two adjacent reconstructions. All reconstructions are done with the same phase recovery sequence from a bispectrum truncated according to Eq. (13), but accessing different subsets of the bispectrum corresponding to truncation parameters of $M = 1$, $M = 2$, $M = 3$ (top row from left to right), $M = 5$, $M = 7$ and $M = 10$ (bottom row from right to left).

Figure 7 demonstrates how the reconstructed image depends on the amount of bispectrum information used; i.e., on the truncation parameter M in Eq. (13). It can clearly be seen that the quality of the result increases significantly when M is raised from 1 to about 5, while larger values of M do not yield better results (see the discussion in Sect. 2.4).

Figure 6 shows how a poor phase recovery sequence, detected by its asymmetric phase number and phase consistency diagrams, can cause artificial structures in the reconstructed image. In this case, a second star is created at a position just opposite (with respect to the center of the image) of the actual β Scorpii. The reconstructions shown in Fig. 5 were obtained with a truncation parameter $M = 5$. For the granulation data, the typical rms contrast of a single frame is 4...5 %, while the average picture has 3 % rms. The reconstruction has a contrast of 11 %, so the gain in resolution is substantial.

5. Discussion and conclusions

The enormous size of the four-dimensional speckle masking bispectrum exceeds the main memory capacities of all today's computers and thus must be drastically reduced. Making use of the inherent bispectrum symmetries reduces the bispectrum size by a factor of 12, without any loss of information. Further truncation of the bispectrum implies a loss of information in theory, but reconstructions of high quality can still be achieved practically.

We have shown that both the amount of information retained in a truncated bispectrum as well as the phase recovery sequence influence the resulting reconstruction. The improvement of the reconstructed picture when increasing the truncation parameter M from 1 to 2 is most striking (see Fig. 7). This can be the result of either the increase of bispectrum phases that contribute

to a given Fourier phase or the increase in the frequency range over which phase closure relations are established, which would reduce effects of anisoplanatism. The $M = 1$ reconstruction presented in Fig. 7 resembles a Knox-Thompson reconstruction of the entire field (VDLP), which indicates that anisoplanatism may be the main cause for the difference. The reconstructed picture converges to a stable, unique solution when M increases. There are little differences seen when M is larger than 5, which is certainly specific for the data set studied.

The sequence of bispectrum access influences the resulting reconstruction. We propose phase number diagrams as very useful tools for designing a phase recovery sequence. A phase number diagram should be symmetric, and should be at a maximum close to the frequency origin in order to weigh most heavily the phases that are best known. One of the phase recovery algorithms discussed here has this property (cf. Fig. 6). We found that phase number diagrams are indispensable during development stages for tracing bugs in our speckle masking code.

Once a useful phase recovery sequence is found, phase consistency diagrams are excellent tools to assess the quality of reconstructed images. Consider the consistency diagrams shown in Fig. 6. The bright area near the center of the diagram indicates the region in Fourier space where phases are reliably recovered. This area coincides approximately with the area that contains Fourier amplitude with a signal-to-noise ratio better than 1. The ellipse extends to approximately 70 % of the diffraction limit of the telescope along its longer axis. The origin of the elongation of the speckle images is not known; most of it is presumably caused by astigmatism of the telescope primary. This is of no concern to us, since we are interested in the development of diagnostics.

We have developed four-dimensional speckle masking image reconstruction code and investigated the effect of various phase recovery sequences on the reconstruction. We have also developed a set of diagnostic tools that permit judgement of the phase recovery sequence and the validity of the recovered phase. We have shown that the four-dimensional speckle masking algorithm can successfully reconstruct diffraction-limited images of extended, low-contrast objects.

Acknowledgements. The authors wish to thank Peter Nisenson from the Center for Astrophysics for supplying the speckle data of β Scorpii. They also thank Gerd Weigelt and Karl-Heinz Hofmann for valuable comments on the paper. Part of this work was done while E. P. held two Summer Research Assistantships of the National Solar Observatory. E. P. would like to thank the community of Sunspot, Sacramento Peak, very much for the warm and co-operative hospitality during these two summers. A travel grant from the International Astronomical Union, Commission 38, is gratefully acknowledged by E. P.

References

Bartelt, H., Lohmann, A.W., Wirnitzer, B.: 1984, *Appl. Optics* **23**, 3121 (abbreviated with **BLW**)
Cornwell, T.J.: 1987, *Astron. Astrophys.* **180**, 269
Freeman, J.D., Christou, J.C., Roddier, F., McCarthy, D.W., Cobb, M.L.: 1988, *J. Opt. Soc. Am. A* **5**, 406
Goad, J.W. (ed.): 1987, *Interferometric Imaging in Astronomy*, Proceedings of the Joint Workshop on High-Resolution Imaging from the Ground Using Interferometric Techniques, Tuscon
Hofmann, K.-H., Weigelt, G.: 1986, *Astron. Astrophys.* **167**, L15
Knox, K.T., Thompson, B.J.: 1974, *Astrophys. J.* **193**, L45
Korff, D.: 1973, *J. Opt. Soc. Am.* **63**, 971
Labeyrie, A.: 1970, *Astron. Astrophys.* **6**, 85
Lohmann, A.W.: 1986, *Optik* **72**, 171
Lohmann, A.W., Weigelt, G., Wirnitzer, B.: 1983, *Appl. Optics* **22**, 4028 (abbreviated with **LWW**)
von der Lühe, O.: 1983, *Astron. Astrophys.* **119**, 85
von der Lühe, O.: 1985a, 'High resolution Speckle Imaging of Solar Small Scale Structure: The Influence of Anisoplanatism', p. 96 in Muller, R. (ed.): *Lecture Notes in Physics*, Vol. 233, Springer-Verlag Berlin
von der Lühe, O.: 1985b, 'Speckle Image Reconstruction of Solar Small Scale Structure Observations', Doctorate Thesis, University of Freiburg, West Germany
von der Lühe, O.: 1985c, *Astron. Astrophys.* **150**, 229
von der Lühe, O.: 1987a, 'Calibration Problems in Solar Speckle Interferometry', p. 9 in Goad (1987)
von der Lühe, O.: 1987b, 'Application of the Knox-Thompson Method to Solar Observations', p. 37 in Goad (1987)
von der Lühe, O., Pehlemann, E.: 1988, 'Speckle Masking Imaging of Extended Sources', p. 159 in Merkle, F. (ed.): *NOAO-ESO Conference on High-Resolution Imaging by Interferometry*, Garching bei München, Part I (abbreviated with **VDLP**)
von der Lühe, O., Zirker, J.B.: 1988, 'Scientific Goals for Solar Interferometry', p. 77 in Merkle, F. (ed.): *NOAO-ESO Conference on High-Resolution Imaging by Interferometry*, Garching bei München, Part I
Neri, R., Grewing, M.: 1987, *Mitt. Astron. Ges.* **70**, 321
Reinheimer, T., Weigelt, G.: 1987, *Astron. Astrophys.* **176**, L17
Roddier, F.: 1986, *Opt. Commun.* **60**, 145
Roddier, F., Gilli, J.M., Vernin, J.: 1982, *J. Optics (Paris)* **13**, 63
Weigelt, G.P.: 1977, *Opt. Commun.* **21**, 55
Weigelt, G., Wirnitzer, B.: 1983, *Opt. Lett.* **8**, 389

This article was processed by the author using Springer-Verlag TEX AA macro package 1989.